Chinese Journal of Aeronautics, (2025), 38(8): 103476

Chinese Society of Aeronautics and Astronautics
& Beihang University
Chinese Journal of Aeronautics

cja@buaa.edu.cn
www.sciencedirect.com

FULL LENGTH ARTICLE

A data-driven methodology to predict ice-induced aerodynamic degradation applied to aircraft tailplane design

Salvatore CORCIONE *, **Agostino DE MARCO**, **Vincenzo CUSATI**

Department of Industrial Engineering, University of Naples Federico II, Naples 80124, Italy

Received 29 July 2024; revised 12 September 2024; accepted 14 October 2024
Available online 10 March 2025

KEYWORDS

Data-driven aerodynamics;
Forward swept tailplane;
Gaussian process regression;
Ice accretion prediction;
Machine learning for icing analysis

Abstract This study presents a data-driven approach to predict tailplane aerodynamics in icing conditions, supporting the ice-tolerant design of aircraft horizontal stabilizers. The core of this work is a low-cost predictive model for analyzing icing effects on swept tailplanes. The method relies on a multi-fidelity data gathering campaign, enabling seamless integration into multi-disciplinary aircraft design workflows. A dataset of iced airfoil shapes was generated using 2D inviscid methods across various flight conditions. High-fidelity CFD simulations were conducted on both clean and iced geometries, forming a multidimensional aerodynamic database. This 2D database feeds a nonlinear vortex lattice method to estimate 3D aerodynamic characteristics, following a 'quasi-3D' approach. The resulting reduced-order model delivers fast aerodynamic performance estimates of iced tailplanes. To demonstrate its effectiveness, optimal ice-tolerant tailplane designs were selected from a range of feasible shapes based on a reference transport aircraft. The analysis validates the model's reliability, accuracy, and limitations concerning 3D ice shapes and aerodynamic characteristics. Most notably, the model offers near-zero computational cost compared to high-fidelity simulations, making it a valuable tool for efficient aircraft design.

1. Introduction

Icing is one of the major causes of flight accidents posing substantial risks to aviation safety.[1,2] Because of ice accretion on aircraft surfaces, lift decreases and drag increases leading to a degradation of aircraft aerodynamic performance and controllability.[3] Aircraft icing influences the flight safety in many ways. Under icing conditions, the aircraft experiences a reduction in the maximum lift coefficient and a decrease in the lift curve slope. Simultaneously, there is an increase in drag and the critical stall speed. If the pilot fails to monitor changes in

* Corresponding author.
E-mail address: salvatore.corcione@unina.it (S. CORCIONE).
Peer review under responsibility of Editorial Committee of CJA

Production and hosting by Elsevier

https://doi.org/10.1016/j.cja.2025.103476
1000-9361

airspeed and climb rate, the aircraft may approach the stall boundary.[3,4] Lampton and Valasek,[5] and Sharma et al.[6] performed some flight dynamics studies highlighting the sensitivity of an iced airplane response to pilot control inputs, and showed the hazard of controlling an iced airplane as if it were clean, whereas Wang et al.[7] proposed an intelligent approach to flight risk prediction due to various icing conditions.

Icing on the wings can result in a reduction of the airfoil stall angle of attack, while tailplane icing, particularly in flap downwash flows, may induce a tailplane stall. These conditions can trigger pitch instability and, ultimately, result in a crash. Asymmetric icing can lead to additional rolling moments imposing limitations on lateral control or resulting in rolling and overturn.[8] Icing has adverse effects on control efficiency.[9] Flight tests demonstrate that tailplane icing can result in significantly increased stick force, reaching hundreds of pounds, making manipulation more challenging. Icing on the rudder's movable structure can lead to stuck rudder surfaces, rendering the aircraft uncontrollable. Additionally, icing on the leading edge of flaps causes premature air separation, reducing flap efficiency.

Active de-icing or anti-ice systems are commonly utilized for aircraft main wings due to their crucial role in providing the majority of the aircraft lift. These systems are employed to prevent potential catastrophic aerodynamic performance degradation. However, when it comes to aircraft tailplanes, CS-25 Section 25.143 requires that the aircraft must be controllable and maneuverable with critical ice accretion during different phases of flight, including minimum take-off speed (V_2), approach, go-around, and landing. When demonstrating compliance with CS-25.143 in icing conditions, the airplane's controllability must be shown with the most critical ice accretion for the specific flight phase. Moreover, before the ice protection system is activated and functioning, the airplane must be controllable in a pull-up maneuver up to a $1.5g$ load factor with the most critical ice accretion. This highlights the importance of evaluating the ice-induced loss in terms of maximum lift coefficients.

In the preliminary stages of aircraft design, when considering the sizing of the empennage, it is common practice to accept the presence of ice formation on the empennage and offset the resulting loss in aerodynamic performance by oversizing the tails. Essentially, while active measures are often taken for main wings, a more passive coexistence strategy is typically adopted for tailplanes to optimize various design considerations. Oversizing the tailplanes leads to additional weight, increased parasitic drag, and higher fuel consumption under all flight conditions. Accurate sizing necessitates a thorough understanding of in-flight ice accretion and its effects on aerodynamic performance. Addressing ice-induced tailplane performance decay will facilitate the development of more ice-tolerant and environmentally friendly aircraft designs, accelerating the adoption of novel and greener configurations.

Currently, in addition to on-site observations, analysis of in-flight icing is primarily conducted through icing wind tunnel experiments and in-flight icing simulations. However, both in-situ and icing wind tunnel experiments require a significant amount of labor and lack flexibility in investigation. In contrast, simulating in-flight icing provides a more efficient and flexible method for analyzing icing, offering the potential for a more comprehensive examination of this phenomenon in aircraft design.

The state-of-the-art in numerical ice accretion relays on 3D solvers of Unsteady Reynolds Averaged Navier-Stokes (URANS) equations. Beaugendre et al.[10] introduced FENSAP-ICE, a modular system designed to calculate ice shapes on 3D geometries efficiently, using field models based on partial differential equations. Hasanzadeh et al.[11] introduced a newly developed two-dimensional ice accretion and anti-icing simulation code, CANICE2D-NS. The method is used to predict iced airfoil shapes and performance degradation with a multistep approach. Montreuil et al.[12] developed a modular icing suite, ONICE3D, based on 3D Navier-Stokes flow solver, coupled with a 3D droplet impingement module and a 3D ice accretion tool, ACCRET3D. Cao et al.[13] presents a numerical simulation method for predicting ice accretions on aircraft wings, focusing on the Eulerian two-phase flow theory. Gori et al.[14] introduced "PoliMIce," a modelling framework developed to perform simulations of ice accretion providing a flexible interface allowing different aerodynamic and ice accretion software to communicate. Li and Paoli [15] presented a comprehensive method for simulating ice accretion on aircraft wings, integrating several models into OpenFOAM to study the effects of ice on aerodynamics. They combined a 3D compressible Navier-Stokes solver, droplet flow, mesh morphing, and thermodynamics into one solver for ice accretion. Despite the high level of accuracy and increasing computational power, fully relying on CFD still makes it prohibitive to integrate such an approach into a step-by-step aircraft Multi-Disciplinary Optimization process. In a recent paper, Page et al.[16] presented the results of the ice accretion on a horizontal stabilizer of a jet transport aircraft calculated using the commercial software Ansys FENSAP-ICE to conduct state-of-the-art three-dimensional multishot in-flight icing simulations.

Despite only the tail being affected by icing in the analysis, while the wing and the rest of the fuselage remained clean, the reported computational expense illustrates the extensive time required for the investigation of a 45-minute holding flight condition in FAR 25 Appendix C cloud conditions. It took one week of wall clock time for the in-flight icing calculations, one day for the clean aerodynamic performance calculation, and another week for the calculation of the iced aerodynamics assessment, all utilizing 140 CPU processes. This highlights once more how the introduction of high-fidelity tools to predict ice accretion and the ice-induced aerodynamic losses would introduce a severe bottleneck into modern complex Multi-Disciplinary Optimization (MDO) workflows.

Several approaches have been implemented to reduce computational costs associated with icing. Hedde and Guffond[17] presented a numerical model developed by ONERA, the French aerospace research center, to simulate the formation and evolution of ice on aircraft surfaces in three dimensions. The model combines a Eulerian approach for the water droplet flow field, a Lagrangian approach for the ice accretion, and a mesh deformation technique for the geometry update. It also accounts for the effects of runback water, surface temperature, and ice shedding, showing good agreement in terms of ice shape, mass, and location.

Li et al.[18] introduced a data-driven approach to quickly evaluate the severity of aircraft icing using the eXtreme Gradient Boosting (XG-Boost) machine learning method. By using a database of 1736 samples consisting of high-fidelity simulation data based on Delayed Detached Eddy Simulation (DDES) and RANS results, they trained, validated, and tested the eXtreme Gradient Boosting (XG-Boost) models. Their model takes the liquid water content, droplet diameter, and exposure time as inputs and outputs the icing severity level, the area covered by ice, and the maximum ice thickness. Jung et al.[19] developed a method for predicting droplet impingement and ice shapes on aircraft surfaces in CFD simulation of in-flight icing by exploiting a Eulerian-based droplet impingement code and a Proper Orthogonal Decomposition (POD) method. A reduced order model, to capture the collection efficiency and the iced shapes on an airfoil has been developed. The proposed method can accurately predict the collection efficiency and the iced shapes for different mean volume diameters, liquid water contents, and angles of attack. Kang and Yee[20] used proper orthogonal decomposition to reduce the dimensionality of ice shape data generated under various icing conditions, and to interpolate the POD coefficients using Radial Basis Functions (RBFs) or Kriging models. Han and Palacios[21] aimed to validate their icing code named LEWICE3D based on the original NASA's code LEWICE.[22] The latter can predict the heat transfer and aerodynamic performance of an iced airfoil in a wind tunnel test. Han and Palacios[21] used a coupled solver that integrates the LEWICE3D ice accretion model with the FUN3D computational fluid dynamics solver. The solver accounts for the thermal effects of ice. accretion on the airfoil surface and the aerodynamic effects of the ice shape on the flow field. A recent work by Massegur et al.[23] presents a framework for developing low-dimensional models for airfoil icing predictions, based on adaptive sampling, proper orthogonal decomposition, and neural networks. The paper uses FENSAP-ICE to simulate ice accretion and aerodynamics for a NACA0012 airfoil under various icing conditions. Then, it applies different methods to reduce the dimensionality of the problem and reconstruct the ice shapes and the aerodynamic performance from a limited number of samples. Other approaches have been developed in the past decades to reduce the computational burden of such a complex discipline by harnessing the potential of quasi-3D approaches. Fujiwara and Bragg[22], Hedde and Guffond[24] developed a quasi-3D algorithm to calculate the aerodynamic flow field by integrating a 3D vortex-lattice code with a 2D viscous solver. Ice shapes and aerodynamics at various wing cross sections are calculated using a 2D droplet trajectory and the LEWICE inviscid icing code. This approach has been checked against the experimental results on the 65%-scale common research model aircraft acquired at the NASA Glenn Icing Research Tunnel. The lift and drag results demonstrate reasonable agreement with the experiment, except in the vicinity of the stall region, and show comparable results to the 3D RANS computation for the case under study.

The above-mentioned works focus on developing methods to reduce the computational costs of predicting ice shape over 2D or 3D wings and estimating the decay of aerodynamic characteristics. However, none of these approaches has been systematically exploited to develop a prediction method for 3D aerodynamic performance under icing conditions of a parametrically defined aircraft horizontal empennage. The study proposed here exploits a mixed-fidelity quasi-3D approach to significantly reduce the computational cost of predicting ice shapes and estimating aerodynamics. By exploring a broad design space of tailplane shapes and icing conditions, as suggested by regulations,[25] the present work develops an ad hoc and reliable Reduced Order Model (ROM), achieving negligible computational costs in practice. The developed prediction method can be seamlessly integrated into a step-by-step aircraft Multi-Disciplinary Optimization (MDO) process, effectively addressing the bottleneck associated with simulating and analyzing ice accretion. The idea of accelerating MDO by using surrogate models of various disciplines has been already addressed in several other works in the past. Relevant examples to this research were provided by Corcione et al.[26,27] who developed surrogate models based on RBFs to predict the aeroelastic effects as well as the aerodynamic performance of innovative tailplane designs.

By drastically cutting the computational costs of predicting the effects of icing on tails, the present effort unlocks the inclusion of another relevant discipline into the aircraft MDO process. This is a key innovation towards the optimization of innovative tailplanes for future ice-tolerant designs that are safer and more environmentally friendly. The rest of the article is organized as follows. Section 2 introduces the quasi-3D technique used to develop the data-driven prediction of ice-induced aerodynamics on 3D swept tailplanes; the section also includes a benchmark to assess the reliability of the method. Section 3 discusses the approach used to develop prediction methods in the form of ROMs and compares the computational burden required to develop such models with the efforts required by high-fidelity CFD tools. Section 4 presents an application of the proposed data-driven model to a design case study; the example demonstrates the horizontal tailplane sizing process, accounting for ice-induced aerodynamic performance degradation. Finally, some conclusions and remarks are discussed in Section 5.

2. A quasi-3D approach to ice accretion modeling

There are three dominant environmental parameters governing the ice accretion phenomena: Medium Volume Diameter (MVD), Liquid Water Content (LWC), and atmospheric temperature (here called T_{ice}) super cooled water droplets in clouds tend to be of different sizes. The MVD range is usually at 2–50 μm. Larger water droplets may exist but require particular conditions. Water droplets with MVDs smaller than 15 μm can be neglected because they tend to flow around the wing surface 145 with air and cannot be collected. The atmospheric temperature (T_{ice}) significantly affects the energy transformation during the icing process. Aircraft icing occurs at temperatures below 0 °C. If the water droplet temperature is much lower (e.g., below 10 °C) than the wing surface, severe convective heat transfer occurs, causing the droplets to immediately freeze into an ice substrate.[28] This is the basic formation mechanism of rime ice. Conversely, horn-shaped glaze ice forms at higher temperatures. Here, collected droplets may not freeze upon impact but instead form a water film that moves along the substrate and freezes at the tip, creating horn-shaped ice on the upper and lower surfaces. Generally, higher temperatures lead to glaze ice, which is more hazardous than rime ice at lower temperatures. The LWC in the air depends on temperature. At very low temperatures, water vapor condenses into ice crystals, resulting in a low LWC state. LWC decreases with increasing Median Volume Diameter (MVD). High LWC levels result in more liquid water collecting on the wing surface, where the unfrozen water film can move toward the rear of the impact zone, forming large horn heights. Therefore, an atmosphere with high LWC is particularly dangerous for flight safety. To consider the effects of the main parameters influencing ice accretion and resulting ice shapes, the methodology proposed in this study aims to utilize a 'quasi-3D' approach. This modelling strategy aims to significantly reduce the time needed to estimate the ice shape and its impact on the aerodynamic behavior of a transport aircraft, parametrically defined horizontal stabilizer. A low time-consuming analysis tool is mandatory to produce hundreds or even thousands of cases required to develop a data-driven prediction method in the form of reduced order model.

The proposed approach is based on a data collection produced by tools executing specific tasks, as depicted by the workflow of Fig. 1. The process starts by defining a reference lifting surface planform in terms of macro design parameters such as span b, aspect ratio AR, taper ratio λ, planform area S, and the sweep angle at the leading edge Λ_{le}. In this work, the lifting surface is discretized into several cross sections, with each section being associated to an airfoil. This set of 'dry' (i.e., non-iced) airfoils is then analyzed using a CFD-RANS solver, specifically Simcenter STAR-CCM+, under specific aerodynamic conditions (such as flight altitude, Mach number, and a range of angles of attack) to generate the required aerodynamic database for input into a nonlinear Vortex Lattice Method (VLM) code. The VLM is then executed to provide 3D data based on 2D, high-fidelity sectional data. Once the 'clean' lifting surface has been investigated, the icing calculation is then executed. That is, a 2D ice accretion prediction code is applied to each of the defined cross sections, taking into account local flow characteristics such as speed, effective incidence angles, and global thermodynamic parameters like the LWC, MVD, flight speed, and exposure time. Once the ice accretion step has been completed, each of the iced cross sections is reanalyzed using a RANS solver. The latter step provides the necessary aerodynamics in icing conditions. The iced airfoil dataset provides input for the VLM code to calculate 3D aerodynamics under icing conditions. Moreover, once the complete set of iced airfoils for the specific wing has been generated, a 3D CAD model of the lifting surface is produced. The process is then concluded by exporting all the necessary data related to clean and iced 3D aerodynamic characteristics. A fast in-house developed code is used in this work to predict ice accretion on airfoils. The proposed approach is based on 2D inviscid methods to simulate the fluid, a Lagrangian formulation to predict droplets trajectories, a layer method[29] to evaluate the heat transfer, and a Messinger model is used to compute the local ice thickness[30] as well as the new ice shape. This one-way coupling process is repeated to simulate the desired exposure in a multi-step approach.[11] This procedure exhibits a satisfying level of accuracy with a reduced computational cost. In a nutshell, the ice accretion workflow

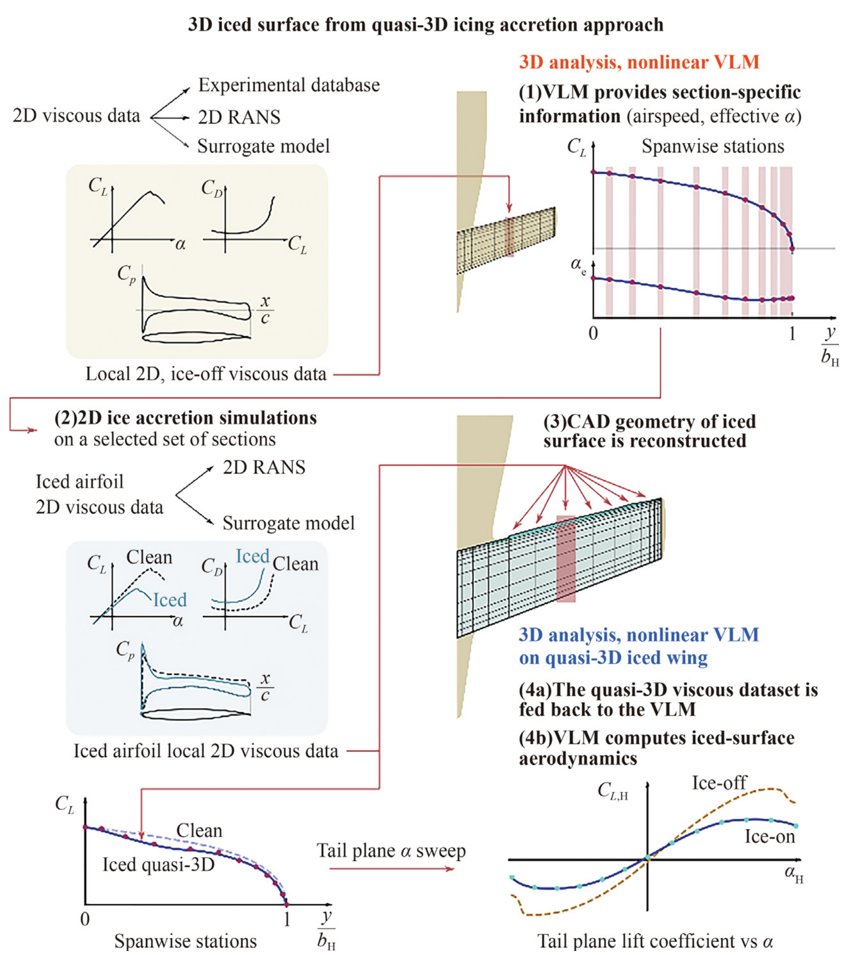

Fig. 1 Logical tree of the proposed quasi-3D approach. Clean and iced aerodynamics of a tailplane.

implemented with the above-described technique follows these steps: (A) Calculating the trajectories of droplets and the local catch efficiency coefficient. (B) Computing the heat transfer coefficient for a rough surface profile. (C) Computing the thermodynamic balance that provides the rate of ice growth and the resulting ice shapes after a specified exposure time. The trajectories are calculated using an explicit method that considers only the drag forces resulting from the velocity difference between the droplet and the surrounding flow field. The collection efficiency is evaluated by calculating the ratio of the mass flow. To take into account for the roughness effects while estimating the heat transfer coefficient, the Makkonen correlation[31] is used. The roughness of the airfoil surface is estimated according to Shin et al.[32] Messinger's equations[30] are used to calculate the local freezing fraction. Starting from the stagnation point the tool solves the steady heat balance equation for each consecutive facet, and then calculated the local equilibrium of the surface temperature, the freezing fraction and then the rate of icing. The unfrozen portion is then allowed to flow back to the nearby surface.

This code can also compute the 2D aerodynamic characteristics in both ice-on and ice-off conditions. However, the code considers the effects of compressibility but not those of viscosity. An improved VLM for fast and reliable aerodynamic predictions,[33] built on classical vortex methods like NASA's,[34] has been adopted to carry out fast and reliable predictions of the 3D aerodynamics. Classical vortex methods suffer from reliability issues limited to the linear 205 lift curve range and assume a fixed lift coefficient slope of 2π based on Glauert theory. The VLM here, based on Blackwell's method,[34] extends results to nonlinear lift regions, including stall, by utilizing experimental data or high-fidelity airfoil curves for aerodynamic load distribution. The method involves two phases: the first utilizes classic VLM to compute spanwise lift and induced angle distributions for a given angle of attack. In the second phase, the VLM's applicability to the nonlinear lift curve range is expanded by accessing an external database of 2D airfoil aerodynamic curves. Adjustments for 3D effects, particularly sweep, are made to the 2D airfoil data.[35] Sweep considerations impact the boundary layer flow backward sweep promotes tip stall, while forward sweep promotes root stall, as evidenced by NACA studies (TN-2445).[36] Estimation of 2.5D aerodynamic characteristics of the wing section perpendicular to the sweep line is done using basic sweep theory, recommended by Mariens et al.[37]

To evaluate the predictive capabilities for ice shapes produced by the application of the proposed approach when a 3D swept wing is considered, some relevant experimental test cases have been selected to perform a comparison. In particular, the test cases AIAA-361 and AIAA-362 from the first AIAA ice prediction workshop database have been selected[38] to serve at this purpose. All the information about the test conditions and all the necessary data are summarized in Table 1, including the geometric features and icing conditions. It is worth noting that for these specific test-cases a restrained CFD-based aerodynamic database has been specifically generated to be compliant with the assigned airfoil, test-case geometries, and aerodynamic conditions. The comparison between the ice shapes at the root and tip section, provided by the experimental test cases, and the computed ones is shown in Fig. 2 and Fig. 3. The charts show three different curves, the green ones represent the experimental shapes, while the blue ones show the results in terms of ice shapes that can be obtained by means of quasi-3D simulation when the aerodynamics of the sections are computed with the same 2D inviscid tool used for the ice accretion. Red curves show instead the ice shapes that can be obtained by a quasi-3D simulation relying on 2D viscous database generated with CFD simulations. A more reliable aerodynamic dataset can provide more accurate local aerodynamics in terms of lift curve variation with respect to the local angle of attack. The latter gives more accurate feeds to the VLM tool, leading to local aerodynamic conditions closer to the experimental ones, this is reflecting on the accuracy of the ice shapes that can be achieved by the proposed approach.

Table 1 Experimental conditions for 3D test cases.

Parameter	CASE 361	CASE 362
MVD (μm)	34.7	34.7
LWC (g/m^3)	0.5	0.5
Mach number	0.32	0.32
Static temperature (K)	257	266
Static pressure (Pa)	92.321	92.321
Water density (kg/m^3)	997	997
Icing time (s)	1 200	1 200
Angle of attack (°)	0	0
Span (m)	2.28	2.28
Sweep at leading edge (°)	30	30
Airfoil	NACA0012	NACA0012

3. Design of experiments on 3D swept horizontal empennages

Since the ultimate goal of this work is the development of a prediction method for the ice-dependent decay of aerodynamic characteristics of a generalized swept tailplane in the form of ROM, there is a need to analyze hundreds of cases under various icing conditions. In order to further reduce the computational cost of running a quasi-3D approach involving 2D CFD-RANS simulations for various wing sections under different conditions, the 2D aerodynamics have been 'surrogated' by developing a dedicated database. A reference airfoil has been selected to serve as the standard cross-sectional profile for all tailplane planform designs under consideration. The chosen reference airfoil is the symmetrical four-digit NACA0009, which is suitable for the tailplane of a transport jet aircraft. This airfoil has been investigated across a broad range of airspeeds, angles of attack, liquid water contents, droplet diameters, air temperatures, and chord lengths by means of high-fidelity two-dimensional CFD simulations. A Design of Experiment (DoE) has been generated by varying all relevant parameters for ice accretion phenomena like air temperature, liquid water content, droplet mean volumetric diameter, Mach number, airfoil chord length and the angle of attack at which the ice shape is computed. Each point of the design space is analyzed over a wide range of angles of attack for both ice-off and ice-on conditions, specifically from −16° to 16°. Due to the high number of costly numerical simulations, the design space has been generated by means of a Latin Hyper-Cube Sampling (LHCS) approach. LHCS is a method for generating a nearly random sample of parameter values from a multidimensional distribution,[39–41] chosen to achieve

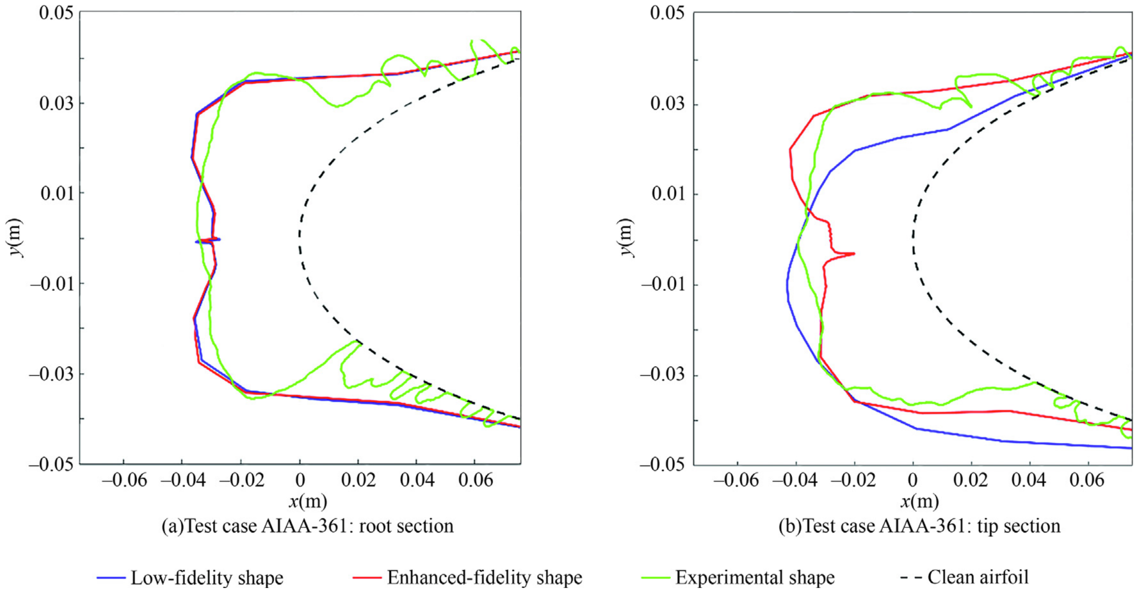

Fig. 2 3D ice shape prediction for test case AIAA-361.

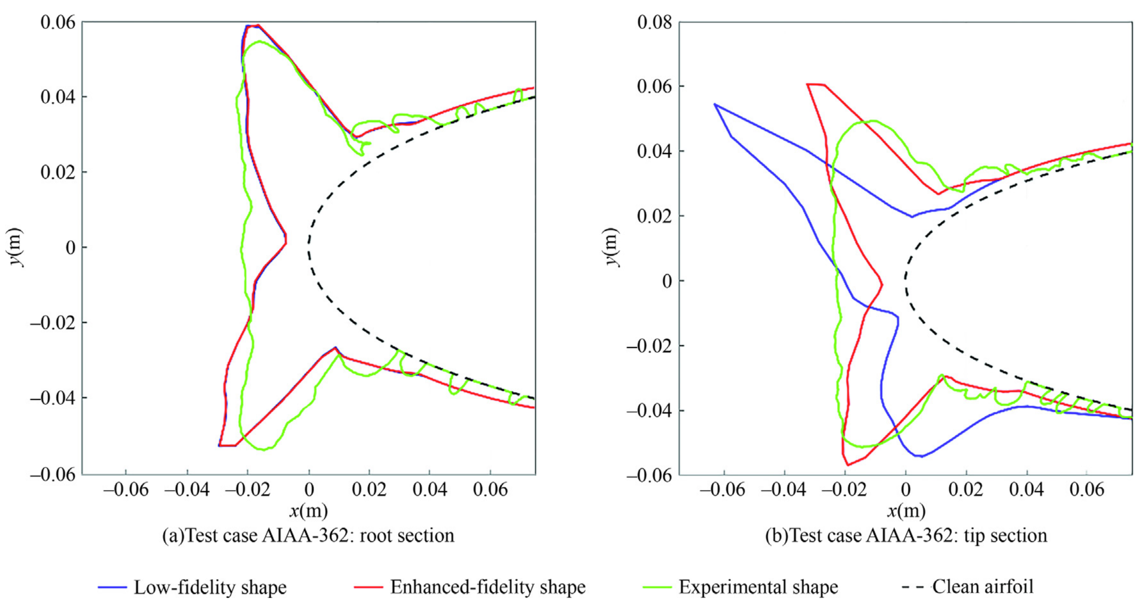

Fig. 3 3D ice shape prediction for test case AIAA-362.

Table 2 Design of experiments for 2D aerodynamics.

Variable	Description	Lower bound	Upper bound
MVD (μm)	Mean volume	15	40
T_{ice} (K)	Temperature	243.15	273.15
Ma_{ice}	Mach number	0.3	0.5
c(m)	Chord length	0.8	4.5
α_{ice} (°)	Angle of attack for ice accretion	0	6

maximum coverage of the design space with a reduced number of sample points.

Table 2 resumes all variables envisaged into the DoE and their lower and upper bounds. The values for the airfoil chord length are conceived to cover a wide spectrum of chord length distributions that could potentially represent the tailplane planform of a jet transport aircraft.

Regarding the atmospheric icing conditions, the range of the DoE has been established in accordance with Appendix C of 14 CFR Part 25.[42]

Appendix C provides two different charts representing two scenarios: “continuous maximum” and “intermittent maximum”. These charts essentially show the probable maximum value of cloud water concentration (also known as the LWC) that is anticipated on average over a specific reference distance, based on the temperature and droplet size in the cloud. Generally, continuous maximum conditions are applied to the sizing of ice protection systems for large aircraft, while intermittent maximum conditions are applied to engine ice protection devices.[25] Based on the objectives of this study, the first scenario will be considered. According to Part II of Appendix C to Part 25,[42] the most critical ice accretion for airplane performance and handling qualities during each flight phase must be considered to demonstrate compliance with the relevant airplane performance and handling requirements in icing conditions. To reduce the number of ice accretions that need to be considered, the regulation allows for any of the specified ice accretions to be accepted if it is demonstrated to be more severe than the ice accretion defined for that phase of flight. Additionally, the most severe ice accretion in terms of its impact on handling qualities may be utilized for airplane performance tests, ensuring that any performance differences are conservatively considered. The latter is the main reason behind the common choice to estimate ice buildups on unprotected surfaces during a 45-minute holding condition. In this case, the LWC must be taken from the "continuous maximum" chart without any reduction, assuming the worst-case scenario of a holding pattern occurring entirely within a region of cloudiness with the maximum probable LWC. Given the above, the sampling approach considered in this study aims to encompass the entire range of temperatures, liquid water contents, and droplet mean diameters specified by the "continuous maximum" as well as flight speeds and attitude angles as comprehensively as possible. To reduce the number of simulations required, a 45-minute holding situation has been deemed a sufficiently conservative scenario for assessing the impact of ice on aircraft tailplane aerodynamics.

According to the charts of Appendix C, the LWC values must be constrained by the limitations in terms of MVD and temperature. To introduce the constraints between the sampled variables, a Latin Hypercube Sampling (LHCS) with rejection has been implemented. The best compromise between the number of samples to be analyzed and the coverage of the LWC, MVD and Temperature chart has been achieved by having at least 100 samples laying within the prescribed chart limitations. A representation of the sampling performed in terms of the area covered of the continuous maximum exposure scenario of Appendix C, is shown in Fig. 4.

The data produced has been organized into a multidimensional database, which serves as the data source for a nonlinear 3D Vortex Lattice Method (VLM). Once the set of 2D data for both ice-off and ice-on conditions was established, the developed quasi-3D approach has been used to investigate a large number of possible jet aircraft tailplane planforms under several icing conditions. The aim is to generate enough information to build a prediction method of the ice-induced aerodynamics degradation in the form of Reduced Order Model (ROM). The latter could be exploitable into preliminary aircraft design and optimization processes unlocking the possibility to include a complex and very computational-costly discipline such as the ice accretion. In this study, in addition to the atmospheric icing conditions a set of additional variables will be introduced to investigate over a wide portfolio of potential horizontal tailplane geometries.

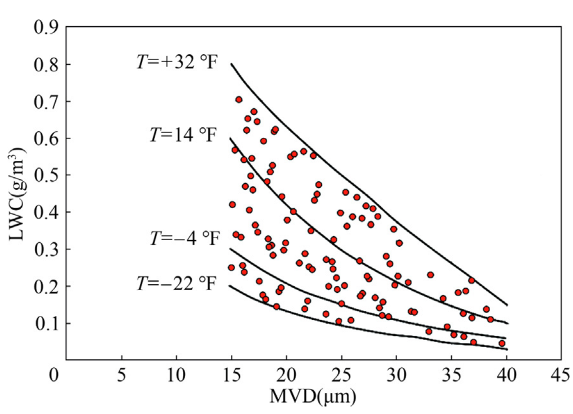

Fig. 4 3D sampling of Appendix C of 14 CFR Part 25 continuous maximum scenario.[42]

The complete list of the exposed design variables and their lower and upper bounds are summarized in Table 3. To drastically cut the computational burden, the tailplane geometries investigated in this DoE will be provided with a single airfoil being the NACA0009. This airfoil has been investigated under several icing conditions and chord lengths, as described in Table 2. A design of experiments consisting of 1 500 cases, encompassing 8 design variables (4 geometrical and 4 aerodynamic parameters) has been generated by means of LHCS approach. For each sampling point, all key aerodynamic characteristics, and their relative variations between ice-off and ice-on have been extracted to reconstruct the tailplane aerodynamic coefficient curves. The stored information deals with the following aspects:

(1) Lift coefficient — to reconstruct the zero-lift angle of attack α_{0L}, the lift coefficient at zero angle of attack C_{L0}, the lift curve slope $C_{L\alpha}$, the stall angle of attack α stall, the maximum lift coefficient $C_{L,\max}$, the angle of attack at the end of the linear range of lift α^*, and the corresponding lift coefficient C_L^*.
(2) Drag coefficient—to estimate the penalty introduced in terms of the minimum drag coefficient $C_{D,\min}$.
(3) Pitching moment coefficient—to evaluate the impact the ice has on the pitching moment coefficient at zero lift C_{M0}.

Several reduced-order models of the degradation of all these aerodynamic characteristics due to ice have been developed as a function of the key geometrical and aerodynamic variables.

3.1. ROM models

Once the DoE has been executed all the aerodynamic characteristics of interest have been collected and prediction methods have been prepared relying on Reduced Order Models (ROM) produced by using the ROM builder capabilities of the commercial software Simcenter Amesim (Advanced Modeling Environment for performing Simulations of engineering systems approach) by SIEMENS.[43] This approach is well suited to work with a sampling pool built on 'scattered' data like the one that has been generated by using the LHCS approach. A Reduced Order Model (ROM) has been developed to predict the aerodynamic performance degradation caused by ice accretion in terms of maximum lifting capabilities for both negative and positive directions, as well as the lift curve slope. Despite the adopted methodology providing a larger list of coefficients of interest, including the drag, and pitching

Table 3 Design space for quasi-3D analysis explorations.

Variable		Description	Lower bound	Upper bound
AR	Geometrical parameter	Tailplane aspect ratio	4	7
S (m^2)		Tailplane area	20	35
Λ_{le} (°)		Leading edge sweep angle	−20	35
λ		Taper ratio	0.25	0.8
Ma_{ice}	Icing condition	Mach number	0.3	0.5
T_{ice} (K)		Temperature	243.15	243.15
MVD (μm)		Water droplet median diameter	15	40
α_{ice} (°)		Angle of attack for ice accretion	0	6

moment coefficients, this study aims to focus on the ice-induced losses in terms of lift. This is motivated by the sizing condition for a tailplane, which pertains to stability and handling qualities. The latter are dominated by the lift curve slope and the maximum lift coefficients. The database generated employing the proposed approach features a finite number p of input space variables, collected in the following array:

$$\begin{aligned} \boldsymbol{x} &= [x_1, x_2, ..., x_p] \\ &= [\mathrm{AR}, S, \Lambda_{le}, \lambda, \alpha_{ice}, Ma_{ice}, \mathrm{MVD}, \mathrm{LWC}, T_{ice}] \end{aligned} \tag{1}$$

whose N samples are arranged in a matrix $\boldsymbol{X}$ of size $N \times p$. For all N simulations, the calculated values of the generic output variable y are stored and arranged in a vector $\boldsymbol{Y}$ of size $N \times 1$.

Exposure time is one of the most critical parameters influencing ice formation, and consequently, the degradation of a lifting surface's aerodynamic performance. The longer the exposure time, the more severe the ice accretion becomes, leading to more pronounced aerodynamic penalties. Although exposure time plays such a significant role, for the purpose of developing the prediction method presented in this study, it has been fixed at 45 min. This specific duration was selected as it represents the most critical scenario under "continuous maximum" icing conditions, in alignment with Appendix C of FAR25. It provides a conservative estimate of the ice-induced penalties on tailplane performance, which is crucial for its preliminary sizing and design evaluation. By focusing on this worst-case scenario, the method aims to offer a robust basis for initial tailplane sizing during early design stages, where detailed information on variable exposure times may not yet be available.

Examples of output variables are the tail maximum and minimum lift coefficient variations due to ice accretion, as well as the lift curve slope. Hence, the output variable y is one of the following variations from ice-off to ice-on conditions (Eqs. (2)–(4)):

$$C_{L,\min}^{ice} = \left(1 + K_{C_{L,\min}}^{ice}\right) C_{L,\min} \tag{2}$$

$$C_{L,\max}^{ice} = \left(1 + K_{C_{L,\max}}^{ice}\right) C_{L,\max} \tag{3}$$

$$C_{L\alpha}^{ice} = \left(1 + K_{C_{L\alpha}}^{ice}\right) C_{L\alpha} \tag{4}$$

The combination of the above defined K_*^{ice} correction factors lead to the efficiency factor η_*^{ice} defined in Eq. (5) that can be calculated as follows:

$$\eta_*^{ice} = \left(1 + K_*^{ice}\right) \tag{5}$$

The 20% of the sampling points have been randomly isolated from the set of samples over the complete design space to serve as a testing dataset. Thus, 1 200 samples have been used to train the ROM model whereas the remaining 300 samples have been used to validate the prediction model. ROM builder by Simcenter Amesim software offers the possibility of generating a predicting method by leveraging different approaches: (A) Response Surface Models (RSM), (B) Gaussian Process (GP) and (C) Neural Network (NN).

Response Surface Models (RSM) are polynomial models that describe algebraic relationships between inputs $\boldsymbol{x}$ and outputs y. They can address problems with multiple inputs (N_x) and outputs by mapping them using polynomial functions of the inputs. The following model equation:

$$y_k = \sum_{i=1}^{N_{mon}} \left(C_i \prod_{j=1}^{N_x} \left(x_j - \bar{x}_j\right)^{O_{ij}} \right) \tag{6}$$

presents a generic output formula for an RSM model. The polynomial consists of N_{mon} monomial terms, where each ith term is a product of inputs raised to the powers specified by orders O_{ij} and scaled by the corresponding coefficient C_i. The fixed-point coordinates determine the offsets $\bar{x}_j$. The coefficients are identified by solving a least-squares problem.

RSM can be configured with input powers up to order 10 (e.g., $\left(x_j - \bar{x}_j\right)^n$ with $n \leqslant 10$) and cross terms up to order 4 (e.g., $x_1^{n_1} \cdot x_2^{n_2} \cdot ...$, where $n_1 + n_2 + ... \leqslant 4$). However, in most cases, linear, quadratic, or cubic RSM models are sufficient, while also reducing extrapolation issues associated with higher-order models.

Neural networks are a type of non-linear regressor that can model the complex relationships between inputs and outputs by being trained on large datasets. These networks are composed of multiple layers, each containing a fixed number of units, also known as neurons. The first layer, called the input layer, corresponds to the number of system inputs, while the final layer, the output layer, matches the number of system outputs. The layers between them, referred to as hidden layers, vary in size depending on the number of neurons they contain. The input and output layers are automatically defined, leaving only the hidden layers to be configured. The network architecture and its hyper-parameters is defined by

(1) The number of hidden layers (from 1 to 6).

(2) The number of inter-connected dense layers, excluding input and output layers. This number usually depends on the complexity of the function to be mapped. Network with more than one hidden layer are called deep networks.
(3) The number of cells per layer that gives the number of units or cells in each layer. This number increases with complexity of the model typically ranging from 3 up to 40.
(4) The activation function that could be linear, tanh (hyperbolic tangent) or relu (rectified linear unit). The first one should be reserved to linear problems.

A neural network is trained by specifying the number of epochs, which defines how many times the optimizer will iterate through the entire training dataset. Each epoch represents one full pass over the data, during which the optimizer works to minimize the loss function. The loss function, typically represented by the root mean square error, decreases progressively as the optimizer adjusts the network's parameters over successive epochs.

A Gaussian process model[44] is a probabilistic model that can capture both linear and nonlinear input–output relationships. A kernel function and a noise level characterize such a model. The kernel function $\boldsymbol{K}(x, x')$ describes the covariance (similarity) between two inputs, projected to a higher dimensional space. The Gaussian process model mean prediction $\bar{y}$ for a generic input x_* is given by

$$\bar{y} = \boldsymbol{K}(x_*, \boldsymbol{X})\left(\boldsymbol{K}(\boldsymbol{X}, \boldsymbol{Y}) + \sigma_n^2\boldsymbol{I}\right)^{-1}\boldsymbol{Y} \tag{7}$$

where $\boldsymbol{K}$ is the $(N \times N)$ kernel matrix, $\boldsymbol{X}$ is a matrix of inputs from the training dataset, σ_n is the noise level, $\boldsymbol{I}$ is the identity matrix, and $\boldsymbol{Y}$ is the above defined column matrix of collected outputs. The projection of the inputs to a higher dimensional space allows Gaussian process models to capture nonlinear relationships between inputs and outputs. This is also known as the 'kernel trick' and it is used in several machine learning algorithms.

Some of the most commonly used kernel functions to calculate $\boldsymbol{K}$ in Eq. (7) are: (A) the Gaussian or squared exponential, which provides smooth fit and is continuously differentiable; (B) the exponential, often used to fit non-smooth outputs thanks to its exponentially decaying covariance; (C) the linear, i.e. the simplest kernel, which leads to linear regression in a Bayesian setting; (D) the "Matern Type 5", that represents a generalization of the Gaussian and exponential kernels, which is suitable for nonsmoothed outputs. These kernels have two hyperparameters: the variance σ and the length scale l.

The fidelity of the models is assessed on the training and validation sets, and various kernel functions are utilized. To maximize the Gaussian Process (GP) model's performance and predictive accuracy, the optimisation of hyperparameters is crucial. The key hyperparameters in a GP model are the following:

(1) Length scale (l): Determines the smoothness of the GP. It defines how far apart input points need to be for their outputs to be considered correlated.
(2) Noise variance (σ_n): Accounts for noise in the data. A higher noise variance allows the model to tolerate noisy observations.

These hyperparameters dictate how well the reduced-order model can capture the relationships between the input parameters and the lower-dimensional output space. All these parameters have been optimized by maximizing the Log Marginal Likelihood (LML) by means of a conjugate gradient-based minimization process.

An example of hyperparameters set obtained after training several ROM models for the output variable $K_{C_{L,\max}}^{\text{ice}}$ (variation of positive maximum lift coefficient from ice-off to ice-on conditions) is reported in Table 4. The kernel variance, length scale, and noise level are also reported. Training durations are also reported, and they are quite fast, as the models are trained on a dataset consisting of 1 200 training samples and 300 testing samples. The input variables are the design variables listed in Eq. (1), while the output variable is the degradation of the finite wing's maximum positive lift coefficient. All models are trained on a single CPU core.

By inspecting Table 4, it turns out that the best ROM to predict $K_{C_{L,\max}}^{\text{ice}}$ is the one marked as "ROM 3", which relies on a Static Gaussian Process (SGP) with an Exponential (Exp) kernel. The same selection process has been applied to the remaining outputs listed in Eqs. (2) and (4). The hyperparameters of the best models for each of the investigated coefficients are reported in Table 5. These data confirm that, for this study, ROMs based on SGP with Exponential kernels are the most effective, both in terms of training and validation metrics.

Hence, the best ROMs for the current study are constructed by adopting an exponential covariance function $k_{\exp}(x, x')$, defined as

$$k_{\exp}(x, x') = \sigma^2 \exp\left(-\frac{\| x - x' \|^2}{2l^2}\right) \tag{8}$$

where σ^2 is the variance parameter, l is the length scale parameter, and $\| x - x' \|$ denotes the distance between x and x' in the input space. Given a set of N training data points $\boldsymbol{X} = [x_1, x_2, \ldots, x_N]$ and corresponding output values $\boldsymbol{y} = [y_1, y_2, \ldots, y_N]$, the covariance matrix $\boldsymbol{K}$ is constructed as $K_{ij} = k\exp\,(x_i, x_j)$, for $i, j = 1, 2, \ldots, N$.

The ROM based on Gaussian processes approximates the true function $f(x)$, expressing the dependence of one of the variables on inputs Eqs. (2)–(4), using a linear combination of kernel functions evaluated at the training data points:

$$f(x) \approx \sum_{i=1}^{N} \alpha_i k_{\exp}(x, x_i) \tag{9}$$

where $\boldsymbol{\alpha} = [\alpha_1, \alpha_2, \ldots, \alpha_N]^{\mathrm{T}}$ is a set of weights. The vector of weights α is found by solving the system of linear equations: $\boldsymbol{K\alpha} = \boldsymbol{Y}$. Once the weights $\boldsymbol{\alpha}$ are determined, the ROM can be used to predict the function value at any new input point x_* as

$$\hat{f}(x_*) = \sum_{i=1}^{N} \alpha_i k_{\exp}(x_*, x_i)$$

The fidelity levels of each trained ROM are highlighted by the regression charts of Fig. 5 and Fig. 6, where the true and predicted values are plotted against the ideal regression for both the training and testing dataset.

All models have been exported as S-functions for use in the MATLAB Simulink environment. From there, it can be

Table 4 Several examples of ROMs predicting $K^{\mathrm{ice}}_{C_{L,\max}}$, variation of positive maximum lift coefficient from ice-off to ice-on conditions. Summary of model parameters. The best trained model is the ROM 3.

Model name	ROM 3	ROM 2	ROM 10	ROM 4	ROM 9	ROM 5	ROM 8	ROM 6	ROM 7	ROM 11	ROM 1
Type of model	Static Gaussian process	Static response surface model	Static neural network	Static Gaussian process	Static neural network	Static Gaussian process	Static neural network	Static neural network	Static neural network	Static neural network	Static response surface model
Training fidelity (%)	95.28	91.72	91.84	91.31	91.16	90.00	90.93	87.79	88.55	89.28	91.98
Validation fidelity (%)	91.84	86.84	85.47	84.94	84.66	84.22	83.61	83.58	82.75	82.55	82.55
Kernel	Precise Exp.	Exp.	–	Exp.	–	Exp.	–	–	–	–	–
Kernel variance	1.73	–	–	39.08	–	123.33	–	–	–	–	–
Noise level	0	–	0	–	–	0	–	–	–	–	–
Fitting method	Subset of regressors	–	–	Subset of regressors	–	Subset of regressors	–	–	–	–	–
Training duration (s)	100	0	4	13	5	13	4	1	2	7	0
Total trained epochs	–	–	50	–	50	–	50	50	50	50	–
Number of layers	–	–	3	–	2	–	2	1	1	3	–
Layer type	–	–	Dense Dense Dense	–	Dense Dense	–	Dense Dense	Dense	Dense	Dense Dense Dense	–
Number of cells	–	–	29 5 3	–	28 8	–	24 4	19	21	31 7 5	–
Activation types	–	–	relu relu relu	–	tanh tanh	–	tanh tanh	tanh	tanh	relu relu relu	–
Training method	–	–	Levenberg-Marquardt	–	Levenberg-Marquardt	–	Levenberg-Marquardt	Levenberg-Marquardt	Levenberg-Marquardt	Levenberg-Marquardt	–
Learning rate	–	–	–	–	–	–	–	–	–	–	–
Batch size	–	–	–	–	–	–	–	–	–	–	–
Adaptive learning	–	–	–	–	–	–	–	–	–	–	–
Data shuffling	–	–	False	–	False	–	False	False	False	False	–
Max order of inputs	–	3	–	–	–	–	–	–	–	–	2
Max order of terms	–	3	–	–	–	–	–	–	–	–	2
Number of coefficients	–	220	–	–	–	–	–	–	–	–	55
Minimal size	–	False	–	–	–	–	–	–	–	–	False
Fixed point	–	False	–	–	–	–	–	–	–	–	False

Table 5 Hyperparameters of the best ROM models for each aerodynamic coefficient.

Hyper parameter	$K^{ice}_{C_{L,max}}$	$K^{ice}_{C_{L,min}}$	$K^{ice}_{C_{L\alpha}}$
Type of model	SGP	SGP	SGP
Training fidelity (%)	95.28	93.5	92.02
Validation fidelity (%)	91.84	90.6	89.45
Kernel	Precise Exp.	Precise Exp.	Precise Exp.
Kernel variance	1.73	2.2	1.85
Noise level σ_n	0	0	0
Fitting method	Regressors	Regressors	Regressors
Training duration (s)	100	95	157

recompiled or exported for various Simulink-compatible targets using Simulink coder or Embedded coder. By feeding the model a vector containing the design variables reported in Eq. (1) exposed in this research, the required output can be calculated.

These models can be easily integrated into a workflow to estimate the decay of aerodynamic characteristics under icing conditions. They can serve various purposes. For example, ROMs can be exploited for a fixed tailplane design under various icing conditions to ensure compliance with regulations, helping to identify the most critical conditions that reduce tail lift capabilities. Alternatively, they can be integrated into a MDO workflow to account for ice-induced aerodynamic degradation under specific icing conditions. This integration helps evaluate the impact of key geometric design variables towards a more ice-tolerant tailplane design.

The charts of Figs. 7 and 8 provide an example of this kind of application. The effect of the sweep angle and air temperature, under a fixed set of all other parameters such as the tail aspect ratio, taper ratio, reference area, and median diameter of the water droplets, has been evaluated. It is worth noting that the LWC is a function of air temperature and MVD to comply with the chart of Appendix C of 14 CFR Part 25 (see Fig. 4). Results clearly highlight the impact that the sweep angle may have on designing a more ice-tolerant tail arrangement. This example highlights how the introduction of ROMs, which are computationally efficient (excluding training costs and data production computational burden), can unlock the possibility of incorporating complex and expansive disciplines into Multi-Disciplinary Optimization (MDO) workflows, as proposed by Corcione et al.[27] to enhance and expedite the development of innovative configurations for more fuel-efficient aircraft.

3.2. Overall computational cost analysis and accuracy assessment of the proposed methodology

The primary objective of this study was to develop a rapid and reliable method to integrate ice accretion modeling into aircraft Multi-Disciplinary Optimization (MDO) workflows, aiming to evaluate designs with enhanced ice tolerance. This objective was accomplished by generating extensive data and organizing these databases to obtain several response surfaces, which are computationally cost-effective. While the computational cost of running a ROM is negligible, the data production necessary for training these models imposes a significant computational burden. It is essential to compare the time required for a comprehensive high-fidelity ice accretion simulation and an aerodynamic behavior assessment across various angles of attack under ice-free and iced conditions with the time needed to develop and execute the ROMs. Data regarding the high-fidelity approach are sourced from Page et al.[16] Table 6 provides a detailed comparison of the computational demands associated with these approaches.

Data shown in Table 6 indicates that the time required to set up, run, and post-process a single case study using the most accurate numerical approach is comparable to the time needed to generate a large dataset for training a prediction method based on response surface methodology. It is clear that the proposed approach could be a viable solution to unlock the possibility of incorporating icing into complex Multidisciplinary Design Optimization (MDO) processes, where hundreds or even thousands of different aircraft designs need to be explored.

To assess the accuracy of the proposed approach, Table 7 compares the ice-induced degradation of aerodynamic charac-

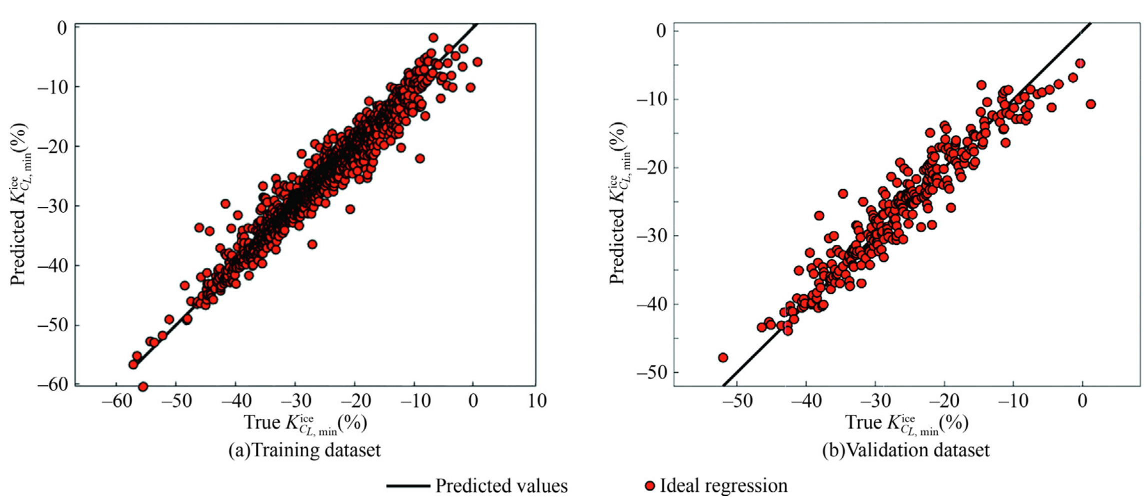

Fig. 5 $K^{ice}_{C_{L,min}}$ validation plot: true vs predicted values.

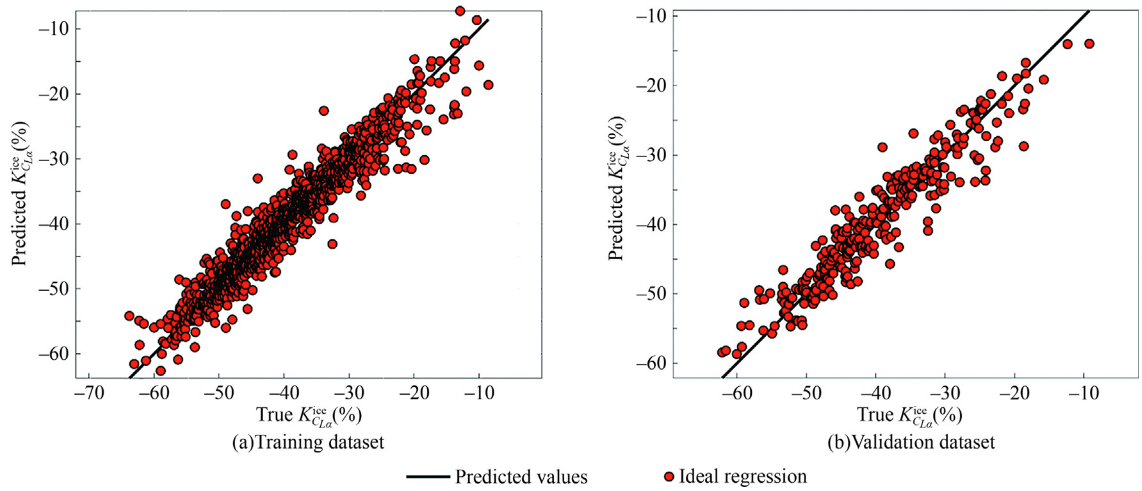

Fig. 6 $K^{ice}_{C_{L\alpha}}$ validation plot: true vs predicted values.

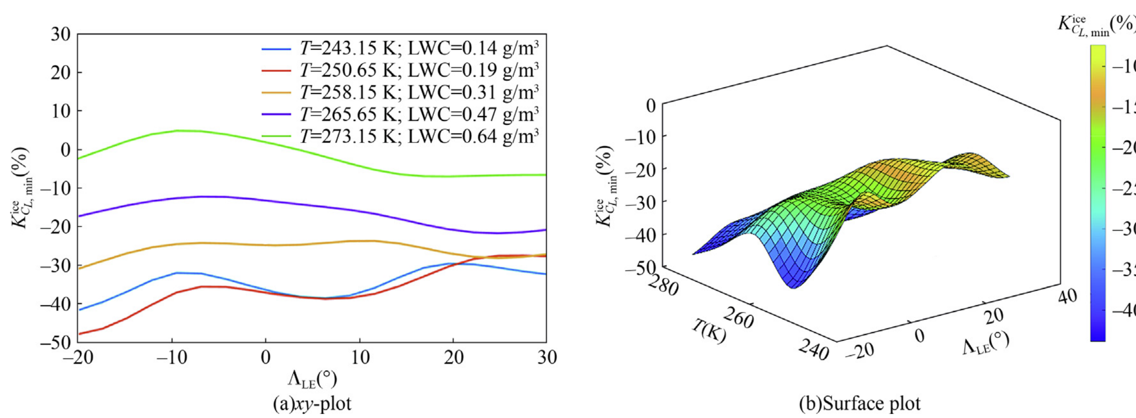

Fig. 7 Effect of tailplane sweep angle and air temperature on $K^{ice}_{C_{L,\min}}$ under a fixed set of parameters: AR = 5.5; S = 31.0 m^2; λ = 0.35; α_{ice} = 4°; Ma_{ice} = 0.45; MVD = 20 μm; LWC as a function of temperature and MVD according of the chart of Appendix C of 14 CFR Part 25. $K^{ice}_{C_{L,\min}}$ validation plot: true vs predicted values.

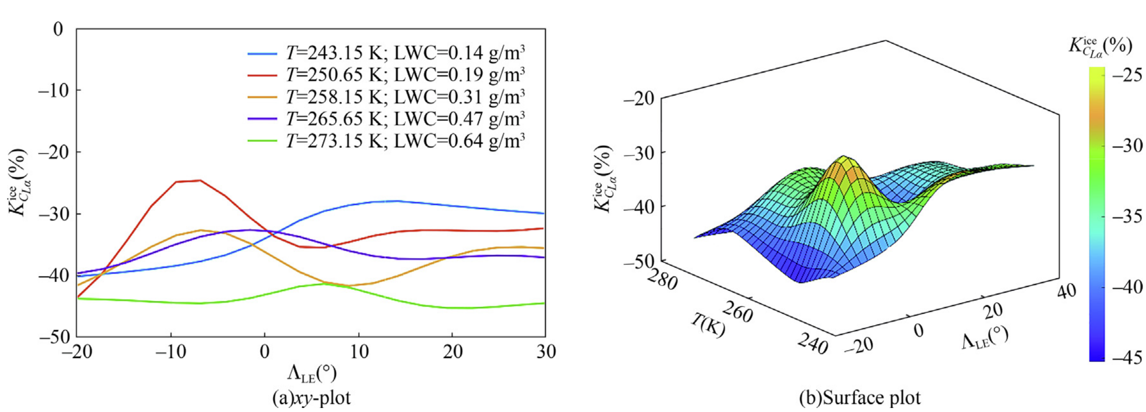

Fig. 8 Effect of tailplane sweep angle and air temperature on $K^{ice}_{C_{L\alpha}}$ under a fixed set of parameters: AR = 5.5; S = 31.0 m^2; λ = 0.35; α_{ice} = 4°; Ma_{ice} = 0.45; MVD = 20 μm; LWC as a function of temperature and MVD according of the chart of Appendix C of 14 CFR Part 25. $K^{ice}_{C_{L\alpha}}$ validation plot: true vs predicted values.

Table 6 Comparison of computational costs between CFD from Page et al.[16] and the proposed approach.

ROMs preparation			
Task	No. of cases	Average time per case (s)	Time (s)
2D ice shape	100	5	500
2D CFD ice-off	100	4 000	400 000
2D CFD ice-on	100	4 620	462 000
Quasi-3D ice-off	1 500	36	54 000
Quasi-3D ice-on	1 500	45	67 500
ROMs set-up	10	135	1 350
		Total time (s)	985 350
		Total time (days)	11
CFD analysis			
Task	No. of cases	Average time per case (s)	Time (s)
3D ice shape	1	604 800	604 800
3D ice-off	1	86 400	86 400
3D ice-on	1	604 800	604 800
		Total time (s)	1 296 000
		Total time (days)	15

Table 7 Comparison of percentage variation of aerodynamic coefficient between CFD results from Page et al.[16] and the proposed ROM model for forward swept tailplane case study.

Coefficient		CFD	ROM
$C_{L,\min}$	Ice-off	−0.677	−0.512
	Ice-on	−0.477	−0.346
$K^{\text{ice}}_{C_{L,\min}}$ (%)		−29.53	−33.00
$C_{L\alpha}$ (1/(°))	Ice-off	0.058 6	0.052 9
	Ice-on	0.045 1	0.035 7
$K^{\text{ice}}_{C_{L\alpha}}$ (%)		−22.96	−32.05

teristics, specifically, the maximum negative lift coefficient and the tailplane lift curve slope, with the findings of Page et al.[16]

4. Icing impact on aircraft tailplane sizing

This section presents a design case demonstrating the sizing process of a horizontal tailplane taking into account the ice-induced aerodynamic performance degradation of the stabilizer itself. It is an application example of the ROM presented in Section 3.1, that shows how effectively the icing effects on tails can be incorporated in early stages of aircraft design.

In preliminary aircraft design stages, the tailplane sizing procedure is based on some relevant aerodynamic requirements, including stability and control. In terms of controllability, the horizontal stabilizer is designed to: (A) ensure an appropriate negative lift coefficient required to reach a required airplane's pitching attitude for landing, and (B) apply the necessary pitch rotation at the end of the on-ground segment during take-off. One of the most important design choices, as an output of the sizing, is the horizontal tailplane area S_{H} or the tail area ratio $S_{\text{H}}/S_{\text{W}}$, where S_{W} is the main wing planform area, which is usually fixed in an earlier stage by mission requirements.

The quantitative equations used in the design process are based on the schematic of forces and moments acting on the aircraft shown in Fig. 9. This picture features an aircraft center of gravity shifted forward, which is an important condition for tailplane sizing, when the airspeed is medium-slow, and the horizontal tail must provide an adequate downforce for equilibrium nonpitching flight. As usual, all longitudinal coordinates x originating at the leading edge of the wing Mean Aerodynamic Chord (MAC), are divided by $\bar{c}$ and made nondimensional, that is, $\bar{x} \equiv x/\bar{c}$.

The effects of icing on tail aerodynamic behavior are often overlooked during the preliminary sizing phase, but in more detailed investigations these effects can lead to significant changes in the tailplane shape and, eventually, to weight penalties. However, designers always reach for an optimal tail size variation to improve empennage aerodynamic efficiency and achieve aircraft performance gains through fuel burn and lower weight.

This research introduces a tailplane sizing process that accounts for the effects of icing on the stabilizer's aerodynamic performance. The proposed method is based on the following two sizing criteria (see function f_1 and f_2 below, and Fig. 10), which are used to determine the tailplane area S_{H} for a given wing-body configuration of reference area S_{W}:

(1) Control limitation criterion, equilibrium at landing (implicit formulation)

$$\frac{S_{\text{H}}}{S_{\text{W}}} \geq \frac{1}{\eta^{\text{ice}}_{C_{L\alpha}}} \cdot \frac{\bar{x}_G - \bar{x}^{\text{LND}}_{\text{ac,WB}} + K^2_{\text{V}} \frac{C^{\text{LND}}_{\text{Mac,WB}}}{C^{\text{LND}}_{L,\max,\text{WB}}}}{\eta_{\text{H}} K^{\text{LND}}_{\text{H}} \frac{l_{\text{H}}}{\bar{c}} \left[\left(1 - K_{\text{GE}} \frac{\mathrm{d}\epsilon}{\mathrm{d}\alpha}\right) + \frac{K_{\text{H}} K^2_{\text{V}} K_{C_{L\alpha,\text{H}}}}{C^{\text{LND}}_{L,\max,\text{WB}}} \left(i_{0,\text{H}} + \tau_{\text{e}} \delta_{\text{e}} - \alpha^{\text{LND}}_{0,\text{W}} \right) \right]} \stackrel{\text{def}}{=} \frac{1}{\eta^{\text{ice}}_{C_{L\alpha}}} f_1(\bar{x}_G) \tag{10}$$

obtained from Fig. 9 by neglecting the tail focal moment coefficient $C_{\text{Mac,H}}$, assuming the landing requirement as the most severe, with the following engineering coefficients $K_V = V^{\text{LND}}/V^{\text{LND}}_{\text{stall}} = 1.2$ (speed factor at landing), $K_{\text{GE}} = 0.9$ (ground-effect factor), $K^{\text{LND}}_{\text{H}} = C^{\text{LND}}_{L\alpha,\text{H}}/C^{\text{LND}}_{L\alpha,\text{WB}}$ (lift curve slope ratio), and

$$K_{C_{L\alpha,\text{H}}} = \frac{1}{1 + K_{\text{H}} \frac{S_{\text{H}}}{S_{\text{W}}} \left(1 - \frac{\mathrm{d}\epsilon}{\mathrm{d}\alpha}\right)} \tag{11}$$

representing the tailplane's effect on the aircraft total lift curve slope $C_{L\alpha}$, influenced by factors such as tailplane incidence angle, wing zero-lift angle of attack, elevator deflection, and elevator efficiency.[45]

(2) Stability limitation criterion, neutral point in cruise:

$$\frac{S_{\text{H}}}{S_{\text{W}}} \geq \frac{1}{\eta^{\text{ice}}_{C_{L\alpha}}} \cdot \frac{\bar{x}_G - \bar{x}_{\text{ac,WB}} + \Delta\bar{x}_{\text{SSM}}}{\eta_{\text{H}} K_{\text{H}} \left(1 - \frac{\mathrm{d}\epsilon}{\mathrm{d}\alpha}\right) \left(\bar{x}_G - \bar{x}_{\text{ac,H}}\right)} \stackrel{\text{def}}{=} \frac{1}{\eta^{\text{ice}}_{C_{L\alpha}}} f_2(\bar{x}_G) \tag{12}$$

where $\eta^{\text{ice}}_{C_{L\alpha}} = 1 + K^{\text{ice}}_{C_{L\alpha}}$ is a correction factor such that accounting for the icing effects on the tailplane.

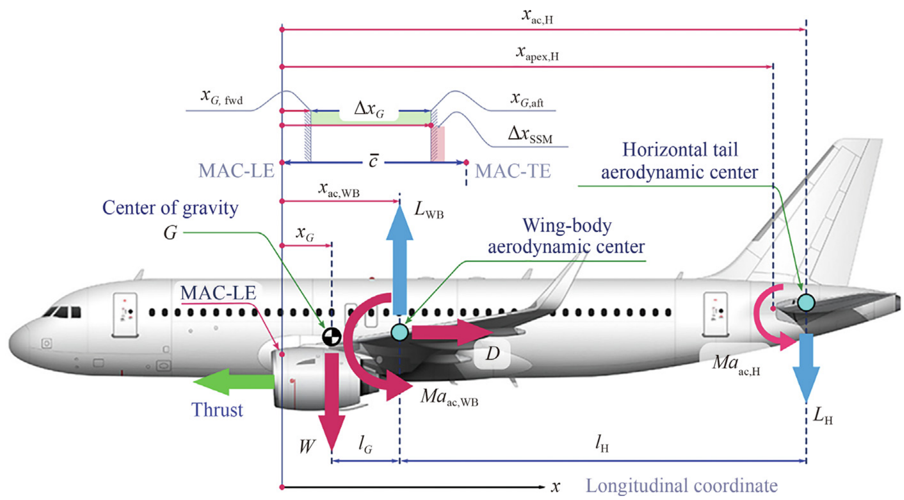

Fig. 9 Forces, moments, longitudinal coordinates, and lever arms used to calculate the pitching moment of an aircraft. Typical situation in which the aircraft center of gravity is shifted forward, the flight speed is medium-slow, and the horizontal tail provides a negative lift at equilibrium. 3D sampling of Appendix C of 14 CFR Part 25,[42] continuous maximum scenario.

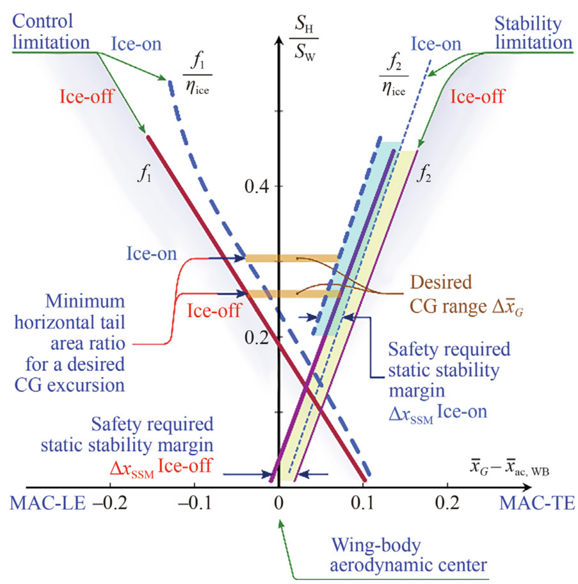

Fig. 10 A typical scissor plot diagram of a large airplane, used to calculate the minimum required horizontal tail area S_H, accounting for control and stability limitations in both cases of ice-off and ice-on; see Eqs. (10), (12), and (13). The abscissas represent the center-of-gravity offsets with respect to wing-body aerodynamic center in cruise.

$$\left(\frac{S_H}{S_W}\right)_{\text{ice-on}} = \frac{1}{\eta^{\text{ice}}_{C_{L\alpha}}}\left(\frac{S_H}{S_W}\right)_{\text{ice-off}} \tag{13}$$

The common practice for determining the tail area during the preliminary sizing stage is to use the Eqs. (10) and (12) to calculate the tailplane area ratio S_H/S_W after having established: (A) the maximum allowable aft location $\bar{x}_{G,\text{aft}}$ ($> x_{\text{ac,WB}}$, but less than the neutral point of a prescribed amount $\Delta\bar{x}_{\text{SSM}}$ named safety static stability margin), (B) a desired center of gravity excursion $\Delta\bar{x}_G$ ($>$ 0, coming from previous design considerations), and hence (C) a maximum forward location $\bar{x}_{G,\text{fwd}} = \bar{x}_{G,\text{aft}}$. The tailplane area S_H is then determined by entering a scissor plot diagram, such as the one shown in Fig. 10, where the tailplane area ratio is plotted against the nondimensional difference $\bar{x}_G - \bar{x}^{\text{cruise}}_{\text{ac,WB}}$; the latter might be positive or negative depending on the aircraft balancing conditions. The icing effects result in modified slopes of the functions f_1 and f_2 in the scissor plot diagram. Iced horizontal stabilizers exhibit a reduced absolute value of their minimum lift coefficient $C^{\text{ice-on}}_{L,\min,H}$ and a reduced lift curve slope $C^{\text{ice-on}}_{L\alpha,H}$.

In Fig. 10 are also reported the two limiting functions f_1/η_{ice} and f_2/η_{ice}, which are used to determine the tailplane area required to meet the stability and control requirements in icing conditions. As a reference aircraft an A320 like platform has been selected. The key geometrical parameters have been extracted from the publicly available data and three-view of the aircraft. The top view of the aircraft is shown in Fig. 11. The figure also reports the comparison with a reference advanced rear-end arrangement that has been investigated in a European research project called IMPACT. The main characteristics of the reference aircraft are summarized in Table 8. The innovative concept introduces a forward-swept horizontal tailplane connected to the fuselage's tail. This configuration contributes to a reduction in structural weight and aerodynamic drag, thereby enhancing the aircraft's fuel efficiency.[26,27] The investigation focuses on developing an innovative tail arrangement to enhance ice tolerance while minimizing the tailplane's planform area. The goal is to design a tailplane that maintains stability and control across a center of gravity travel range wider than that of the reference tail.

Designs of Experiments (DoEs) have been created by varying the same tailplane design parameters used to generate the reduced-order models. To avoid trivial solutions that rely solely on moving the tail backward to increase its lever arm, the tail's $x_{\text{apex,HTP}}$ and $x_{\text{apex,FSHTP}}$ have been fixed to their reference values as reported in Table 8. Two distinct DoEs, each comprising 100 000 samples, have been generated using a LHCS procedure. The first DoE investigates positive sweep tails exclusively, while the second explores negative sweep tail

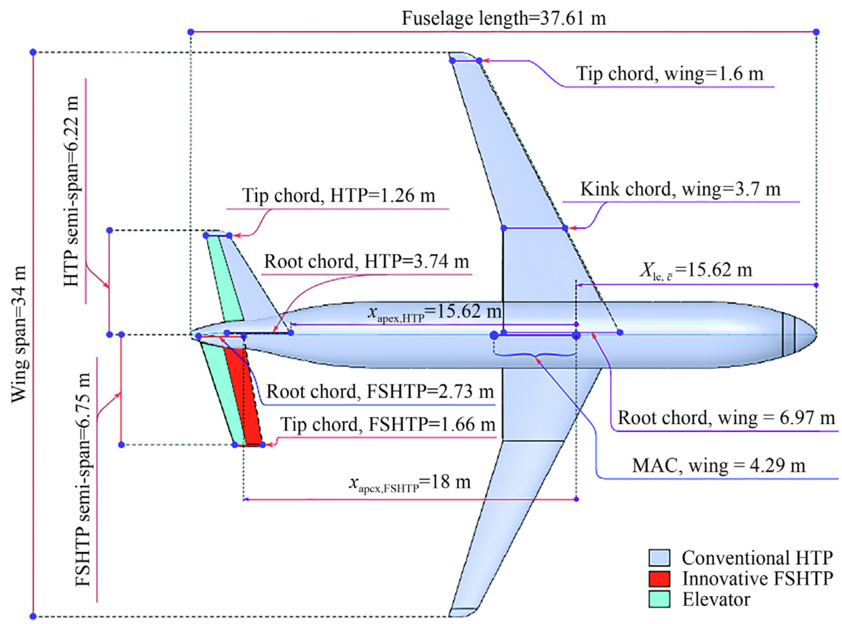

Fig. 11 Top view of reference aircraft: conventional positive swept tail and innovative rear end with a negative swept empennage.

Table 8 Reference aircraft characteristics.

Symbol	Value	Unit	Description
S_W	125	m^2	Wing planform area
S_H	31.36	m^2	Reference tailplane planform area
$\bar{c}$	4.29	m	Wing Mean Aerodynamic Chord (MAC)
l_H	17.19	m	Wing-tail aerodynamic centre distance
$C_{L,\max,\mathrm{WB}}$	1.337		Wing-body maximum lift coefficient
$C^{\mathrm{LND}}_{L,\max,\mathrm{WB}}$	2.84		Wing-body maximum lift coefficient at landing
$\bar{x}_{ac,W}$	0.25		Position of the wing aerodynamic centre
W_{MTO}	724.9	kN	Maximum take-off weight
$\bar{x}_{G,fwd}$	0.17		Maximum forward position of centre of gravity (% of wing MAC)
$\bar{x}_{G,aft}$	0.37		Maximum afterward position of centre of gravity (% of wing MAC)
$x_{apex,HTP}$	15.62	m	Position of the tail root leading edge of the conventional tail
$x_{apex,FSHTP}$	18	m	Position of the tail root leading edge of the conventional tail

Table 9 Objective functions, variables, and constraints.

Function	Variable
Objective function No. 1	Maximize $(\Delta\bar{x}_G)_{\text{ice-on}}$ as % of MAC
Objective function No. 2	Minimise $\frac{S_H}{S_W}$
With respect to	AR_H, S_H, Λ_{le}, λ
Subject to	$\frac{S_H}{S_W} - \left(\frac{S_H}{S_W}\right)_{ref} \leqslant 0$
	$\left(\bar{x}_{G,fwd} - \bar{x}_{G,fwd}\right)_{\text{ice-on}} \leqslant 0$
	$\left(\bar{x}_{G,aft} - \bar{x}_{G,aft}\right)_{\text{ice-on}} \geqslant 0$

arrangements. The statement of the investigated problem is mathematically described in Table 9.

The chart in Fig. 12 shows the resulting scissor plot for the reference conventional tailplane. The control condition at landing is represented by the solid red line, while the stability condition is shown as a solid black line. Dashed lines represent ice-on conditions, where the tailplane's lifting capabilities are reduced due to ice-induced performance decay, as estimated through the proposed reduced-order models. Grey dots represent all solution that have been rejected since they are not compliant with all the prescribed constraints.

To facilitate the identification of solutions that meet the imposed conditions, the investigated points have been plotted on a plane where the abscissa represents the maximum available center of gravity nondimensional excursion ($\Delta\bar{x}_G = \bar{x}_{G,aft} - \bar{x}_{G,fwd}$), and the ordinate represents the tail-to-wing planform area ratio. This plane allows for the identification of a Pareto front, as illustrated by the red solid line in Fig. 13.

Notably, in the case of a conventional positive swept tail, no significantly better solutions than the reference one are identified. However, for the forward swept tail, several solutions exhibit more ice tolerant behavior than the reference tail arrangement. Additionally, many feasible solutions indicate a reduced tailplane area. According to the Pareto front in the right panel of Fig. 13, a designer can select from various tailplane arrangements based on specific design criteria. For instance, two alternative forward swept tail solutions have been selected from the depicted Pareto front: the first corresponds to the minimum tail planform area (indicated by the magenta square), and the second provides the largest center of gravity travel in ice-on conditions (represented by the green square on the chart). These solutions are shown and compared with the reference conventional tail arrangement in Fig. 14.

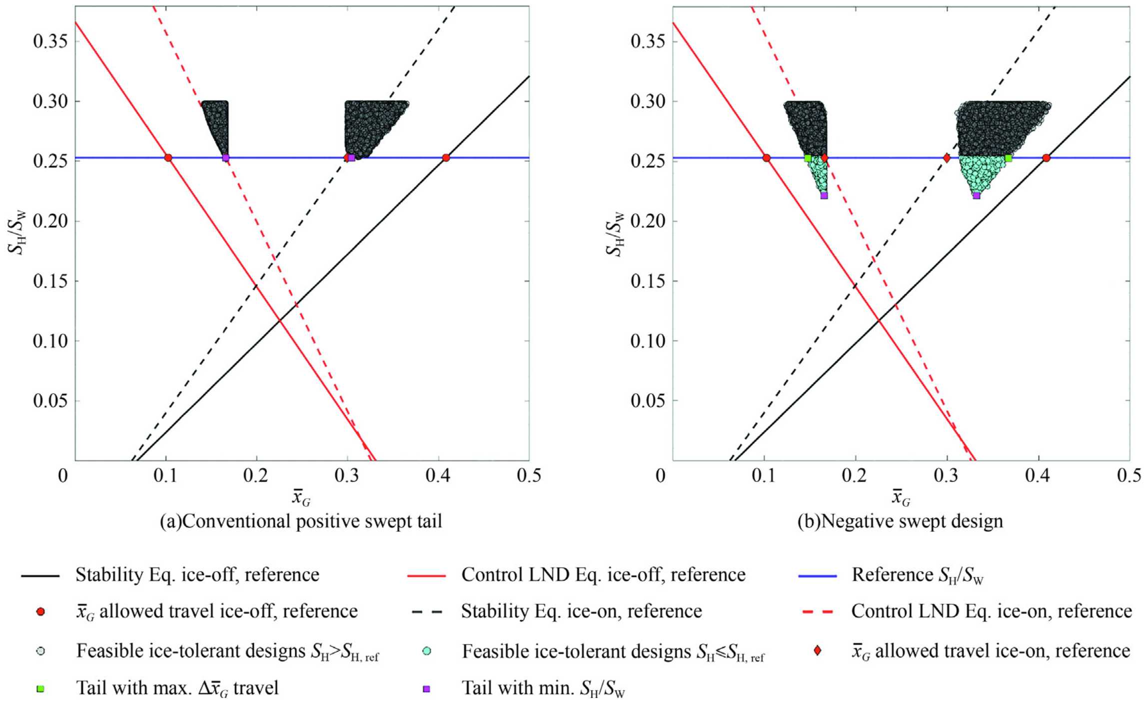

Fig. 12 Scissor plot for a more ice tolerant tailplane design. ice-on indicates conditions with ice accretion whereas ice-off relates to ice-free conditions.

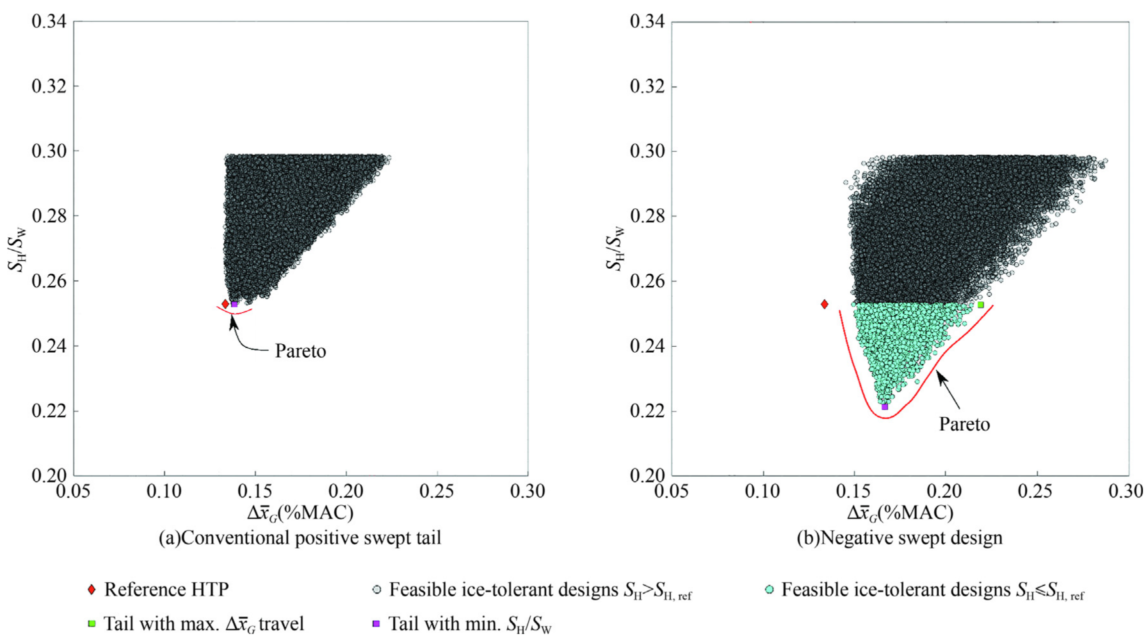

Fig. 13 Pareto fronts for a more ice tolerant tailplane design.

The tailplane design process discussed in this study is not exhaustive as it primarily addresses stability requirements and landing control (conditions (1) and (2) outlined in Eqs. (10) and (12)). A more comprehensive tail sizing process is influenced by other factors,[46] such as tailplane incidence and elevator deflection.

The tailplane needs to generate significant downward lift, achieved either through a high negative tailplane angle of attack or elevator deflection, as well as a lesser amount of upward lift. Critical flow conditions at the tail may arise, particularly in scenarios where the flaps are in the landing position and the center of gravity is at the most forward location during a push-over maneuver at low airspeed (e.g., following an initial pull-up in a baulked landing or during a stall recovery maneuver). Therefore, it is relevant to estimate the tail's maximum negative lift coefficient ($C_{L,\min}$) and the corresponding angle of attack (the negative stall angle).

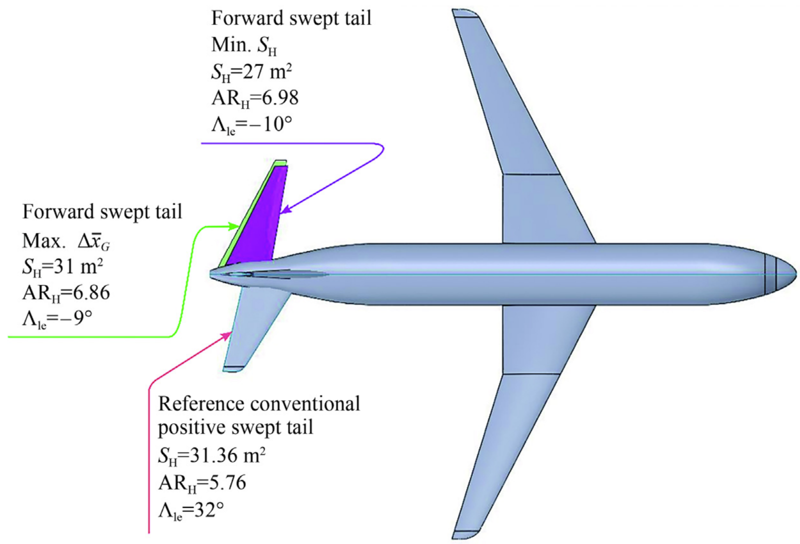

Fig. 14 Top view of reference aircraft and two innovative ice-tolerant tail arrangements. Tail in green: design with the largest center of gravity range under icing conditions; tail in magenta: design with the minimum tail planform area.

Although these characteristics have not been explicitly reported in this work, the developed reduced order models (ROMs) also encompass these parameters. The comparison of the tailplane stall angle, $C_{L,\min}$, and $C_{L\alpha}$ is presented in Table 10 for further analysis.

The proposed exercise illustrates a potential application of the developed ROMs. This example highlights that incorporating ice accretion considerations into aircraft multidisciplinary optimization is feasible only if fast and reliable methods are available. In this respect, the proposed approach represents a significant advancement, accelerating the development of innovative, safer, and more ice-tolerant tailplane designs.

5. Conclusions and further developments

This study has introduced a data-driven approach for predicting tailplane aerodynamics in icing conditions and demonstrated its application to the ice-tolerant design of aircraft horizontal stabilizers. The core innovation lies in a low-computational-cost model for analyzing the effects of icing on swept and tapered planforms, leveraging an extensive multi-fidelity data gathering campaign. This method integrates seamlessly into aircraft design multi-disciplinary optimization workflows, offering a cost effective yet reliable predictive tool essential for contemporary aerospace engineering challenges.

Table 10 Icing effects on the proposed tailplanes characteristics.

Parameter	$\alpha_{\text{stall}}(°)$	$C_{L,\min}$	$C_{L\alpha}(1/(°))$
HTP (reference)	−6	−0.35	0.035
FSHTP, max. $(\Delta\bar{x}_G)$	−7	−0.53	0.051
FSHTP, min. S_H/S_W	−8	−0.52	0.055

The predictive approach, based on a comprehensive dataset of iced airfoil shapes obtained using well-established 2D inviscid methods, spans a wide range of operational parameters. High-fidelity computational fluid dynamics simulations further enriched this dataset, encompassing both clean and iced geometries across diverse flight conditions. These results were systematically organized into a multidimensional aerodynamic database. The utilization of this 2D database within a nonlinear vortex lattice method enabled the prediction of the three-dimensional aerodynamic characteristics of lifting surfaces, culminating in a quasi-3D model. This reduced-order model delivers rapid aerodynamic performance estimates of iced lifting surfaces, proving to be a pivotal tool in ice-tolerant aircraft design.

The practical application of the proposed model was demonstrated through a detailed design study of the Airbus A320-like tailplane, comparing conventional and forward-swept configurations. The forward-swept tailplane configuration showcased the model's potential to expand the aircraft design space. Specifically, the forward-swept tailplane could either reduce the tailplane surface while maintaining the same center of gravity excursion or maintain the same surface area while allowing for a larger center of gravity excursion under icing conditions. This versatility underscores the capability of forward-swept configurations to enhance design efficiency and performance.

In conclusion, the proposed model has proven its reliability and accuracy in predicting the aerodynamic characteristics of iced lifting surfaces, with negligible computational cost compared to high-fidelity numerical analyses. The application to tailplane design demonstrated the model's value towards industrial practical needs. The findings of this research pave the way for further exploration and refinement of ice-tolerant designs, with implications for enhancing aircraft safety and performance in adverse weather conditions. Furthermore, the open-access availability of these models ensures that the scientific community can leverage the presented findings to advance research and development in the field of aircraft icing.

CRediT authorship contribution statement

Salvatore CORCIONE: Writing – review & editing, Writing – original draft, Visualization, Validation, Supervision, Software, Resources, Project administration, Methodology, Investigation, Funding acquisition, Formal analysis, Data curation, Conceptualization. **Agostino DE MARCO:** Writing – review & editing, Writing – original draft, Visualization, Validation, Supervision, Software, Data curation. **Vincenzo CUSATI:** Writing – review & editing, Writing – original draft, Validation, Methodology, Investigation, Data curation.

Declaration of competing interest

The authors declare that they have no known competing financial interests or personal relationships that could have appeared to influence the work reported in this paper.

Acknowledgement

This article has received funding from the Department of Industrial Engineering, University of Naples Federico II, Italy.

References

1. Reehorst A, Chung J, Potapczuk M, et al. Study of icing effects on performance and controllability of an accident aircraft. *J Aircr* 2000;**37**(2):253–9.
2. Cao YH, Wu ZL, Su Y, et al. Aircraft flight characteristics in icing conditions. *Prog in Aerosp Sci* 2015;**74**:62–80.
3. Cole J, Sand W. Statistical study of aircraft icing accidents. *29th aerospace sciences meeting*. Reston: AIAA; 1991.
4. Gent RW, Dart NP, Cansdale JT. Aircraft icing. *Philos Trans r Soc London A: Math Phys Eng Sci* 2000;**358**(1776):2873–12829.
5. Lampton A, Valasek J. Prediction of icing effects on the dynamic response of light airplanes. *J Guid Contr Dyn* 2007;**30**(3):722–32.
6. Sharma V, Voulgaris PG, Frazzoli E. Aircraft autopilot analysis and envelope protection for operation under icing conditions. *J Guid Contr Dyn* 2004;**27**(3):454–65.
7. Wang GZ, Xu HJ, Pei BB. An intelligent approach for flight risk prediction under icing conditions. *Chin J Aeronaut* 2023;**36**(6):109–27.
8. NTSB. In-flight icing encounter and loss of control Simmons airlines, d.b.a. American Eagle Flight 4184, Avions de Transport Regional (ATR) model 72-212, N401AM. Washington, D.C.: NTSB; 1996. Report No.: NTSB/AAR-96/02.
9. Wilder RW. A theoretical and experimental means to predict ice accretion shapes for evaluating aircraft handling and performance characteristics. Pairs: AGARD; 1978. Report No.: SEEN 79-15036 06-05.
10. Beaugendre H, Morency F, Habashi WG. Development of a second generation in-flight icing simulation code. *J Fluids Eng* 2006;**128**(2):378–87.
11. Hasanzadeh K, Laurendeau E, Paraschivoiu I. Quasi-steady convergence of multistep Navier–Stokes icing simulations. *J Aircr* 2013;**50**(4):1261–74.
12. Montreuil E, Chazottes A, Guffond D, et al. ECLIPPS: 1. Three-dimensional CFD prediction of the ice accretion. *1st AIAA atmospheric and space environments conference*. Reston: AIAA; 2009.
13. Cao YH, Ma C, Zhang Q, et al. Numerical simulation of ice accretions on an aircraft wing. *Aerosp Sci Technol* 2012;**23**(1):296–304.
14. Gori G, Zocca M, Garabelli M, et al. PoliMIce: A simulation framework for three-dimensional ice accretion. *Appl Math Comput* 2015;**267**:96–107.
15. Li SB, Paoli R. Modeling of ice accretion over aircraft wings using a compressible OpenFOAM solver. *Int J Aerosp Eng* 2019;**2019**(1):4864927.
16. Page J, Ozcer I, Zanon A, et al. IMPACT: Numerical study of aerodynamics of an iced forward-swept tail with leading edge extension. *SAE technical paper series*. 2023.
17. Hedde T, Guffond D. ONERA three-dimensional icing model. *AIAA J* 1995;**33**(6):1038–45.
18. Li SB, Qin JK, He M, et al. Fast evaluation of aircraft icing severity using machine learning based on XGBoost. *Aerospace* 2020;**7**(4):36.
19. Jung SK, Myong RS, Cho TH. Efficient prediction of ice shapes in CFD simulation of in-flight icing using a POD-based reduced order model. *SAE technical paper series*. 2011.
20. Kang YE, Yee K. Temporal prediction of ice accretion using reduced-order modeling. *J Korean Soc Aeronaut Space Sci* 2022;**50**(3):147–55.
21. Han YQ, Palacios J. Validation of a LEWICE-based icing code with coupled heat transfer prediction and aerodynamics performance determination. *9th AIAA atmospheric and space environments conference*. Reston: AIAA; 2017.
22. Fujiwara GE, Bragg MB. 3D computational icing method for aircraft conceptual design. *9th AIAA atmospheric and space environments conference*. Reston: AIAA; 2017.
23. Massegur D, Clifford D, Da Ronch A, et al. Low-dimensional models for aerofoil icing predictions. *Aerospace* 2023;**10**(5):444.
24. Hedde T, Guffond D. Improvement of the ONERA 3D icing code, comparison with 3D experimental shapes. *Proceedings of the 31st aerospace sciences meeting*; 1993 Jan 11–14 ; Reno, NV, USA. Reston: AIAA; 1993.
25. Jeck RK. Icing design envelopes (14 CFR Parts 25 and 29, Appendix C) converted to a distance-based format, Regulation. Atlantic City (NJ): Federal Aviation Administration; 2002. Report No.: DOT/FAA/AR-00/30.
26. Corcione S, Cusati V, Memmolo V, et al. Impact at aircraft level of elastic efficiency of a forward-swept tailplane. *Aerosp Sci Technol* 2023;**140**:108461.
27. Corcione S, Mandorino M, Cusati V. Beyond conventional: An integrated aerostructural optimization approach for innovative tailplane configurations. *Aerosp Sci Technol* 2024;**150**:109242.
28. Li HR, Zhang YF, Chen HX. Optimization design of airfoils under atmospheric icing conditions for UAV. *Chin J Aeronaut* 2022;**35**(4):118–33.
29. Kays WM, Crawford ME, Weigand B. Convective heat and mass transfer. *J Appl Mech* 1967;**34**(1):254.
30. Messinger BL. Equilibrium temperature of an unheated icing surface as a function of air speed. *J Aeronaut Sci* 1953;**20**(12):849–50.
31. Makkonen L. Heat transfer and icing of a rough cylinder. *Cold Reg Sci Technol* 1985;**10**(2):105–16.
32. Shin J, Berkowitz B, Chen H, et al. Prediction of ice shapes and their effect on airfoil performance. *Proceedings of the 29th aerospace sciences meeting*; 1991 Jan 7–10; Reno, NV, USA. Reston: AIAA; 1991.
33. Della Vecchia P, Nicolosi F, Ruocco M, et al. An improved high-lift aerodynamic prediction method for transport aircraft. *CEAS Aeronaut J* 2019;**10**(3):795–804.
34. Blackwell JAJ. A finite-step method for calculation of theoretical load distributions for arbitrary lifting-surface arrangements at subsonic speeds. Hampton: NASA Langley Research Center; 1969. Report No.: NASA-TN-D-5335.

35. Holt DR. Introduction to transonic aerodynamics of aerofoils and wings. Accuris: ESDU; 2003. Report No.: ESDU 90008.
36. Purser PE, Spearman ML. Wind-tunnel tests at low speed of swept and yawed wings having various plan forms. Langley (VA): Langley Aeronautical Laboratory, NACA; 1951. Report No.: NACA-TN-2445.
37. Mariens J, Elham A, van Tooren MJL. Quasi-three-dimensional aerodynamic solver for multidisciplinary design optimization of lifting surfaces. *J Aircr* 2014;**50**(2):547–58.
38. Ice prediction workshop [Internet]. Reston: AIAA; 2021[cited 2024 Jul 9]. Available from: https://icepredictionworkshop.wordpress.com/cases-files.
39. Tang BX. Orthogonal array-based Latin hypercubes. *J Am Stat Assoc* 1993;**88**(424):1392–7.
40. Owen AB. Orthogonal arrays for computer experiments, integration and visualization. *Statistica Sinica* 1992;**2**(2):439–52.
41. Ye KQ. Orthogonal column Latin hypercubes and their application in computer experiments. *J Am Stat Assoc* 1998;**93**(444):1430–9.
42. Electronic code of Federal Regulations, Appendix C to Part 25 - Atmospheric icing conditions [Internet].Washington, D.C.: NASA; 2024 [cited 2024 Jul 9]. Available from: https://www.ecfr.gov/current/title-14/chapter-I/subchapter-C/part-25/795 appendix-C-to-part-25.
43. Siemens Digital Industries Software [Internet]. Hong Kong: Simcenter AMESIM, version 2023.10 [updated 2023 Oct 16; cited 2024 Jul 9]. Available from: https://plm.sw.siemens.com/en-US/simcenter/systems-simulation/amesim/.
44. Rasmussen CE, Williams CKI. *Gaussian processes for machine learning*. Cambridge(MA): The MIT Press; 2006.
45. Obert E. *Aerodynamic design of transport aircraft*. Amsterdam: IOS Press; 2009.